A framework for pulmonary fissure segmentation in 3D CT images using a directional derivative of plate filter

Hong Zhao[a], Berend C. Stoel[c], Marius Staring[c], M. Bakker[c], Jan Stolk[d], Ping Zhou[b], Changyan Xiao[a,*]

[a] *College of Electrical and Information Engineering, Hunan University, Changsha, 410082, China*
[b] *College of Biology, Hunan University, Changsha, 410082, China*
[c] *Department of Radiology, Leiden University Medical Center, P.O. Box 9600, 2300 RC, Leiden, The Netherlands*
[d] *Department of Pulmonology, Leiden University Medical Center, P.O. Box 9600, 2300 RC, Leiden, The Netherlands*

ARTICLE INFO

ABSTRACT

Imaging pulmonary fissures by CT provides useful information on diagnosis of pulmonary diseases. Automatic segmentation of fissures is a challenging task due to the variable appearance of fissures, such as inhomogeneous intensities, pathological deformation and imaging noise. To overcome these challenges, we propose an anisotropic differential operator called directional derivative of plate (DDoP) filter to probe the presence of fissure objects in 3D space by modeling the profile of a fissure patch with three parallel plates. To reduce the huge computation burden of dense matching with rotated DDoP kernels, a family of spherical harmonics are particularly utilized for acceleration. Additionally, a two-stage post-processing scheme is introduced to segment fissures. The performance of our method was verified in experiments using 55 scans from the publicly available LOLA11 dataset and 50 low-dose CT scans of lung cancer patients from the VIA-ELCAP database. Our method showed superior performance compared to the derivative of sticks (DoS) method and the Hessian-based method in terms of median and mean $F_1 - score$. The median $F_1 - score$ for DDoP, DoS-based and Hessian-based methods on the LOLA11 dataset was 0.899, 0.848 and 0.843, respectively, and the mean $F_1 - score$ was 0.858 ± 0.103, 0.781 ± 0.165 and 0.747 ± 0.239, respectively.

© 2020 Elsevier B.V. All rights reserved.

1. Introduction

The human lungs are recursively subdivided into functional units: at the highest level into the left and right lung, separated by the mediastinum, and subsequently into lung lobes, separated by a double layer of visceral pleura, called pulmonary fissures, then lung segments [1]. The left lung includes two lobes (upper and lower lobe) separated by a single left oblique fissure, while the right lung includes three lobes (upper, middle and lower lobe) separated by a right oblique fissure and a horizontal fissure. Computed tomography (CT) is the current gold standard for lung imaging. Detecting pulmonary fissures in CT images may form the basis for lobe segmentation, but can also be used as an independent imaging biomarker for disease evaluation and treatment planning [2]. Consequently, accurate detection of pulmonary fissures is important for clinical purposes. However, manual segmentation is tedious, time-consuming and suffers from some degree of subjective bias, which motivates the development of automatic algorithms to segment fissures and extract fissure characteristics. In CT images fissures appear as thin surface-like structures with an intensity higher than the surrounding lung parenchyma. However, patient movement, partial volume effects and lung lesions tend to result in low contrast and blurred fissures in CT scans [3]. This problem is more serious in low-dose CT images due to its inferior image quality as compared to normal-dose CT [4]. It may cause missing detection of weakly visible or pathological fissures. Furthermore, false detection may occur due to surrounding anatomical structures (vessels and airways) and lung diseases (bullous lung disease and fibrosis) that may locally resemble fissures. Other challenges for automatic detection of fissures are their inhomogeneous intensities and thin, incomplete and variable structures.

Despite these challenges, many approaches have been proposed in the literature to detect fissures. These approaches may be broadly categorized into learning-based and non-learning-based groups. In the former, Van Rikxoort et al. [5] applied a supervised machine learning method to detect fissures, where 57 features were chosen to train a fissure classifier. Wei et al. [6] used a neural

network to identify fissure regions. Recently, George et al. [7] employed a progressive holistically-nested network (P-HNN) to identify fissures. Gerard et al. [8] designed a FissureNet based on convolutional neural networks to extract fissures. Later, the FissureNet method was extended to a fully automated pipeline for segmentation of lobes [9]. Another two deep learning solutions to the lobe segmentation were presented in [10] and [11]. However, the performance of machine learning methods depends on a large training dataset with ground truth segmentations, which is difficult to obtain, as fissures are hard for a human to delineate in 3D images.

Regarding non-learning-based methods, some researchers incorporated auxiliary structures to identify fissure regions of interest, aiming to reduce false detection and estimate non-visible fissures. Several segmentation frameworks have been designed to integrate information about airways and vessels for fissure localization. Such approaches apply distance transform [12], watershed transform [13–15], voronoi division [16], shortest path [17,18], adaptive sweeping [19], single-atlas [20] and multi-atlas [21] segmentation algorithms. Recently, Bragman et al. [22] proposed a Gaussian Mixture Model (GMM) with a Markov Random Field (MRF) regularization to segment fissures, which depends on the accuracy of inter-patient scans registration. Although these approaches can obtain desirable results in some cases, their performance largely depends on the prior anatomical information. Actually, the most reliable and valuable information still originates from the fissure itself. Therefore, many authors put more effort on the detection of visible fissures and directly use the intensity and shape characteristics of fissures in either 2D slices or 3D CT images to extract and refine fissures, not incorporating auxiliary structures.

In 2D slices pulmonary fissures usually appear as thin curved lines. Thus, some authors directly delineated curved-line structures from 2D images. Generally, these methods use a local operator or local filtering to enhance voxels that lie on these curved lines, and then design a segmentation procedure to extract fissures. In terms of fissure enhancement, an improved VanderBrug operator, a ridge map method and a MLSEC-ST (multi-local level set extrinsic curvature measure with structure tensor analysis) approach have been proposed by Kubo et al. [23], Wang et al. [24] and Zhang et al. [20], respectively. Subsequently, for fissure segmentation, a fuzzy reasoning framework [20] and a shape-based curve growing algorithm [24] are utilized. However, both of the above segmentation frameworks need manual interaction of initializing fissure detections. To automatically segment fissures, Wei et al. [19] proposed an approach using adaptive fissure sweeping and wavelet transform to delineate fissures. Klinder et al. [25] presented a line enhancing (LE) filter using multiple hypotheses testing with an anisotropic kernel, which possesses a large local receptive field to detect fissures. Unfortunately, these approaches do not sufficiently make use of the 3D shape characteristics of fissures, so that they may falsely enhance non-fissure structures (e.g. in a slice parallel to a vessel's main axis, the vessel would appear as a line).

In 3D images fissures appear as locally bright plates, which motivates other researchers to design so-called plateness filters to detect pulmonary fissures. Pu et al. [26] presented a computational geometry method to approximate fissures using a set of plates. Its improved version [27] applied an anisotropic morphological filter to fill small holes in the fissures. Later, this approach was further extended by Gu et al. [28], who utilized a piecewise plane fitting algorithm to directly extract the plate-like structures in the original lung CT images. The key idea of the above approaches is to detect plates or planes in sub-volumes. It can be essentially interpreted as a zero-order plateness filter. Without a difference operation, this filter tends to be disturbed by inhomogeneous background intensities or large area noise. It is well known that Hessian-based second-order plateness filters [3,29] are used more than zero-order filters. Ross et al. [30] presented a particle system which is based

on the multiscale second-order feature to identify candidate fissure points, and subsequently a Maximum A Posteriori (MAP) estimation was used to suppress noise while preserving the fissure feature. Wiemker et al. [31] proposed a plateness filter using structure tensors and Hessian matrices for shape description. Similarly, Lassen et al. [32], Shamonin et al. [33] and Li et al. [34] used eigenvalues of the second-order Hessian matrix to design a plateness filter for detecting fissures. However, the performance of the second-order plateness filters depends on the size of the filter kernel [35]. The filter with small kernel sizes is prone to be interrupted by noise. With large kernel sizes in 3D space, the computational burden of the filter will increase dramatically. To ease this problem, Xiao et al. [36] proposed a simplified solution using a pseudo-3D plate description for fissures detection. Its principle is to detect 2D lines in the axial, sagittal and coronal slices by a set of derivative of stick (DoS) kernels rather than detect plates in 3D space directly. To suppress the adjacent noise, Peng et al. [37] recently proposed an orientated derivative of stick (ODoS) filter, in which they utilized the orientation information of the fissures to purify the pulmonary fissures. Despite their plausible segmentation result, the DoS-based methods cannot detect weak and point-cloud-like fissures (appearing as sparse and slightly bright point set) due to their homogeneous intensity assumption and a lack of a solid coplane constraint.

Motivated by the fact that fissure patches could be locally approximated with a plate in 3D space, we follow a similar idea of the existing DoS filter [36] to determine the presence of fissure objects with an anisotropic derivative operator, namely a directional derivative of plate (DDoP) filter. Different from the original 2D line-segments (i.e. sticks) based filtering, a kernel with triple parallel planes is proposed to directly detect fissure objects in 3D space. To reduce the related heavy computation burden with multiple orientation template matching, a spherical Gaussian derivative is particularly introduced to reformulate the DDoP kernel. Additionally, we present a two-stage post-processing scheme, where an orientation partition and merging algorithm is first employed to generate initial segmented fissures based on the flatness and continuity of fissures, and then, as a compensation for non-flat fissures due to pathological factors, a region growing approach is used to reconstruct the non-flat fissures.

The remainder of this paper is organized as follows. We first retrospect the related fissure detection filters in Section 2. Then, the proposed DDoP filter and the two-stage post-processing procedure are proposed in Section 3. Experiments and evaluation on clinical scans are presented in Section 4. Section 5 includes a discussion and finally the conclusion is derived in Section 6.

2. Retrospect of the fissure enhancement filters

In this section, we retrospect several traditional fissure enhancement filters. In order to compare these filters and understand their limitations, we reformulate them into a convolution filtering framework $f(x) = I(x) * k(x)$, where I is an image and k a filtering kernel. Under this unified framework, these underlying filtering kernels are investigated. This might help to understand the motivation and principle of the proposed method.

In the following sections, the methods mostly related to our filter, such as the plane-fitting [28], Hessian-based [31], directional derivative of anisotropic Gaussian (DDoAG) [38], DoS [36] and ODoS [37] approaches, are briefly reviewed.

2.1. Piecewise plane fitting algorithm

A piecewise plane fitting algorithm was proposed by Gu et al. [28] for the identification of pulmonary fissures, where the thresholded CT image was treated as a cloud of points and the
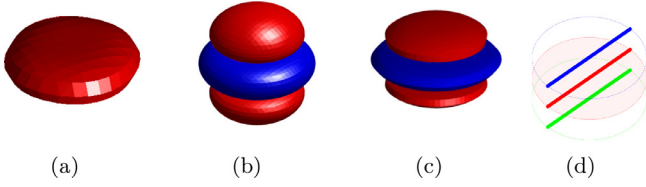
Fig. 1. Illustrations of various filtering kernels. (a)-(d) denotes the 3D kernel of piecewise plane, Hessian, anisotropic scale and DoS filter, respectively. Here, the red color corresponds to the positive regions and the blue color being the negative regions.

lung volume was subdivided into small spherical volumes. It fits a plane in each sub-volume by using an efficient plane fitting algorithm, with the assumption that a pulmonary fissure is locally coplanar. A plane in 3D space was defined as [28]:

$$F = \{p|p \in \mathbf{R}^3, f(p) = 0\},$$
$$f(p) = \cos(\alpha)\sin(\theta)x + \sin(\alpha)\sin(\theta)y + \cos(\theta)z - \rho, \quad (1)$$

where (α, θ, ρ) are the three parameters determining the plane F. This plane fitting algorithm is to find the optimal plane by maximizing the function based on the density of point clouds:

$$\varepsilon(\alpha, \theta, \rho) = \frac{\sum_{f(p_i)^2 < u^2} w_i(u^2 - f(p_i)^2)}{\pi(r^2 - f(o)^2)} \quad (2)$$

where w_i is assigned a value of either 1 (point clouds) or 0 (background), u is related to fissure thickness, $f(p_i)$ represents the distance between point p_i and the plane $F(\alpha, \theta, \rho)$, o and r denote the center and the radius of the sphere, respectively, and $\pi(r^2 - f(o)^2)$ is the cross-sectional area S_a of the plane F with respect to the sphere. It can be seen from the numerator of Eq. (2) that the sum of the product of w_i and $u^2 - f(p_i)^2$ can be reformulated to a convolution form. Thus, Eq. (2) can be rewritten as:

$$\frac{\sum_{f(p_i)^2 < u^2} w_i(u^2 - f(p_i)^2)}{\pi(r^2 - f(o)^2)} = \frac{w * h_p}{S_a} = w * \frac{h_p}{S_a}, \quad (3)$$

where w denotes a binary image, h_p a filtering kernel and S_a a normalizing term.

Observed from Eq. (2), the value of the object function $\varepsilon(\alpha, \theta, \rho)$ depends on the distance of points to the plane F, and only the distance smaller than u is taken into account. Therefore, the value of the kernel h_p is non-negative, and its shape is determined as a plate with a thickness of $2u$ as shown in Fig. 1(a). Since $u^2 - f(p_i)^2$ is a convex quadratic function of the distance $f(p_i)$, along the orthogonal direction of this plate, its profile resembles a bell shape. We call this a zero-order plateness filter, for it works like a smoothing kernel.

Essentially, this zero-order plateness filter works on the assumption that the binarized fissure points concentrate and distribute homogeneously around a central plane. Its plate detection criterion consists in searching for the plate having the maximum weighted average intensity. However, for a fissure with intensity inhomogeneity or the interference close to it, this filter will tend to select the wrong plate.

2.2. Hessian-based filters

The Hessian-based plateness filters [3,29,31,33] are popular for pulmonary fissure detection. This type of method combines the eigenvalues of the Hessian matrix to design a plateness filter for fissure likelihood measurement. Usually, a Gaussian filter is firstly applied to smoothen the original CT scan with an appropriate set of kernel scale σ. At each voxel, the Hessian matrix is then calculated. Assuming its eigenvalues $\lambda_1, \lambda_2, \lambda_3$ with corresponding eigenvectors $\vec{e_1}, \vec{e_2}, \vec{e_3}$ are computed and ordered such that

$|\lambda_1| \leq |\lambda_2| \leq |\lambda_3|$, then the plateness likelihood function is defined as follows [29]:

$$P = \begin{cases} 0, & \text{if } \lambda_3 \geq 0 \\ \max_\sigma (F_A F_B F_S), & \text{otherwise} \end{cases} \quad (4)$$

$$F_A = \exp\left(-\frac{A^2}{2\alpha^2}\right), F_B = \exp\left(-\frac{B^2}{2\beta^2}\right),$$
$$F_S = \left(1 - \exp\left(-\frac{S^2}{2\gamma^2}\right)\right), \quad (5)$$

where $A = \frac{\lambda_2}{\lambda_3}$, $B = \frac{\sqrt{|\lambda_1 \lambda_2|}}{|\lambda_3|}$, $S = \sqrt{\lambda_1^2 + \lambda_2^2 + \lambda_3^2}$, and (α, β, γ) are the free parameters. The eigenvector $\vec{e_3}$ is obtained as the normal orientation of the fissure. This Hessian-based plateness filter is made up of the second-order derivatives of the isotropic Gaussian kernel, whose shape is depicted in Fig. 1(b). Although theoretically this Hessian-based filter is able to detect idealized bright plates on a dark background, its filtering performance to real images depends on the scale of the kernel. The filter with a small kernel size is prone to being interrupted by noise. With a large kernel size, the filter might wipe out the fissures due to the contradiction between the isotropic kernel and the extremely anisotropic fissures.

2.3. DDoAG filter

Several anisotropic Gaussian filters [38,39] were introduced to detect anisotropic objects, such as edges and ridges in 2D images. This type of kernel can also be extended to detect surface-like structures like fissures in 3D images. A 3D anisotropic Gaussian kernel can be formulated as

$$G(\vec{x}, \sigma_\|, \sigma_\perp) = \frac{1}{(2\pi)^{3/2}\sigma_\|^2\sigma_\perp}e^{-\frac{1}{2}\left(\frac{x^2+y^2}{\sigma_\|^2} + \frac{z^2}{\sigma_\perp^2}\right)}, \quad (6)$$

where $\vec{x} = (x, y, z)$ is the spatial coordinate, the value of $\sigma_\|$ determines the scale of an edge or surface detectable by the kernel in the $x - y$ plane, while the value of $\sigma_\perp$ specifies the scale of the kernel in the z direction, which is orthogonal to the $x - y$ plane. As shown in Fig. 1(c), its directional second-order derivative along the z direction may be used as a plate template. Dense matching with rotating templates at a large number of orientations is indispensable to directly detect fissures in 3D images. Although the fast anisotropic Gaussian filtering [40] has been proposed to reduce the computational burden for 2D images, the computation of the dense filtering in a 3D space is still costly.

2.4. DoS filter

As an extreme case of anisotropy, the derivative of stick (DoS) filter was originally proposed by Xiao et al. [36] for pulmonary fissure detection. Its basic principle was to use a group of rotated kernels to probe the presence of fissures in axial, sagittal and coronal slices and merge information from these orthogonal planes to obtain the plateness response. As shown in Fig. 2(a), its kernel consists of three parallel sticks (left, middle, and right) denoted with Ls, Ms and Rs, respectively, where θ denotes the 2D orientation and S is the inter-stick spacing. When the DoS kernel is parallel to the fissure line with the middle stick located on the fissure, it is able to probe the fissure strength by simultaneously measuring the intensity homogeneity $\lambda_\|$ along the middle stick and the intensity difference $\lambda_\perp$ between the middle stick and its neighbors. In order to adapt to different orientations of a fissure, a set of stick templates with different discrete orientations were used to generate the 2D fissure line strength, which was formulated as:

$$F_o = \max(\max_{1 \leq i \leq 2(L-1)}(\lambda_\perp^\theta - k \cdot \lambda_\|^\theta), 0), \quad (7)$$

(a) The DoS kernel   (b) The DDoP kernel
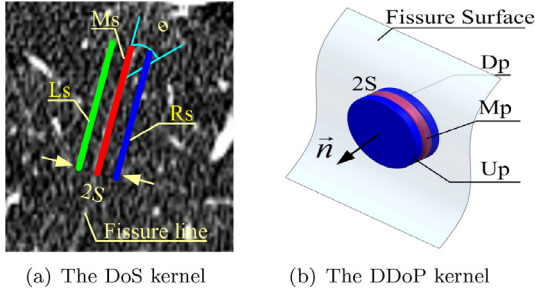
Fig. 2. A comparison of the DoS kernel and the DDoP kernel: Both kernels overlay a fissure. The DoS kernel consisting of three parallel sticks (Ls, Ms and Rs) in 2D space is extended to the DDoP kernel consisting of three parallel plates (Up, Mp, and Dp) in 3D space. The orientation of the DoS kernel is denoted by θ, which is parallel to the fissure line, while for the DDoP kernel denoted by $\vec{n}$, which is orthogonal to the fissure surface. Here, regions rendered in red indicate positive parts of filters, while blue and green indicate negative kernel values.

where $2(L-1)$ is the number of sticks. To achieve multi-section integration, a 3D shape-tuned fissureness function was defined as [36]

$$F^{3D} = (F_o^A + F_o^S + F_o^C) \cdot \frac{median(F_o^A, F_o^S, F_o^C)}{max(F_o^A, F_o^S, F_o^C)}. \tag{8}$$

Here, F_o^A, F_o^S and F_o^C indicate the 2D fissure responses from the axial, sagittal and coronal cross-sections, respectively.
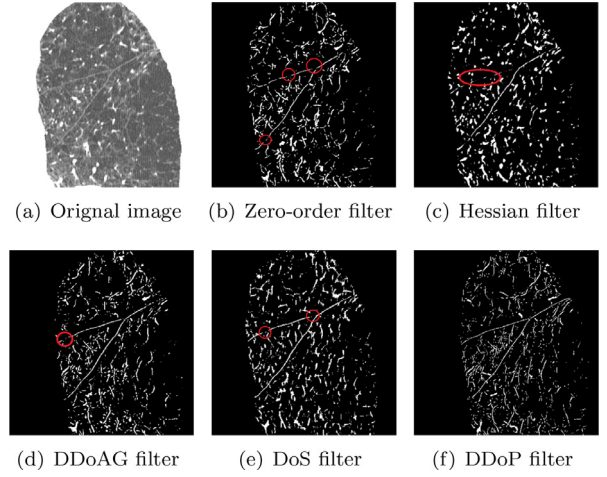
2.5. ODoS filter

As an improvement to the DoS filter, the oriented derivative of stick (ODoS) filter was introduced by Peng et al. [37] to further improve the accuracy and robustness of the fissure detection. Its main idea was to use the fissure's orientation ($cos\ \theta$, $sin\ \theta$) in sagittal slices to purify the fissures. Their orientation field was constructed with

$$\overrightarrow{V}_{sag} = F^{3D} \cdot (\cos\theta, \sin\theta). \tag{9}$$

The DoS-based filter is a simplified method by integrating fissure line responses in three orthogonal cutting planes instead of directly detecting fissure patches in 3D space. Although the ODoS filter can suppress the adjacent noise to some extent, its inherent drawback is that it cannot detect weak fissures due to a lack of a solid coplane constraint.

From the above analysis of existing fissure enhancement filters, we conclude that the higher anisotropy and larger anisotropic context the filtering kernel possesses, the better it performs. This can be confirmed by the filtering results shown in Fig. 3(b)-(e). They are generated from retrospected filters applied to a lung CT scan containing inhomogeneous background and weak fissures (Fig. 3(a)). With respect to the piecewise plan fitting approach, we reimplement it in terms of a convolutional filter, whose filtering response (Fig. 3(b)) is not consistent along the fissure line. The result of the Hessian filter (Fig. 3(c)) shows that the fissure response is seriously interrupted by noise due to a small isotropic kernel. The anisotropic scale filter generates a better filtering result (Fig. 3(d)), while it is costly in computation. The DoS filter gives a suboptimal response to weak and noisy fissures, see Fig. 3(e).

Among these filters, most of them are anisotropic kernels except the Hessian filter using an isotropic Gaussian kernel. Due to the isotropic kernel, the Hessian filter samples a wider adjacent neighborhood, which increases the possibility of introducing more interference. The DoS filter is an extreme case of anisotropy, but this is not a true 3D plate detector, which leads to a limited context lacking inter-slice information. The performance of the zero-order plateness filter is inferior to the anisotropic scale filter, as

(a) Orignal image   (b) Zero-order filter   (c) Hessian filter

(d) DDoAG filter   (e) DoS filter   (f) DDoP filter

Fig. 3. Filtering results for the different kernels applied to the lung CT images using optimized parameters.

the smoothing kernel is less robust to inhomogeneous intensities than the derivative kernel. However, the anisotropic scale filter is impractical to detect fissures due to its highly computational cost for large scale images in 3D space. The limitations of these classical filters inspire us to design a new filter for better fissure detection.

3. Our methodology

To overcome the limitations of traditional fissure detection filters, we present a directional derivative of plate (DDoP) filter for pulmonary fissure enhancement and a two-stage scheme for post-processing detection in this section.

3.1. The proposed DDoP filter

As shown in Fig. 4, in CT images pulmonary fissures appear as extremely anisotropic structures with an intensity higher than the surrounding lung parenchyma. Specifically, fissures are extremely thin in their transverse directions, while flat along their axial directions. Additionally, there are few lung vessels of high intensity in a narrow region surrounding the fissures. The shape and appearance characteristics of fissures, namely the anisotropic plate-like struc-
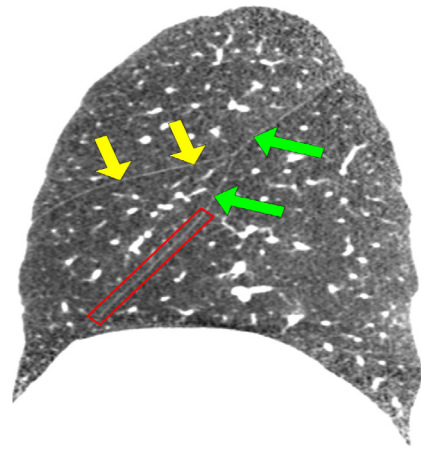
Fig. 4. A sagittal slice of the right lung from a CT image demonstrating the right oblique fissure (green arrows) and the right horizontal fissure (yellow arrows), which appear as bright lines of high intensity crossing the low intensity lung parenchyma. A red rectangle marks a narrow surrounding region of the fissure, where few lung vessels of high intensity appear.
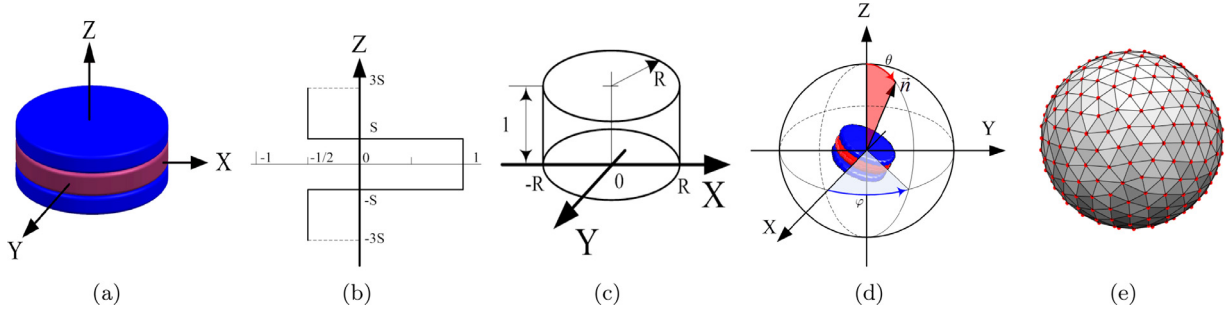
Fig. 5. Illustration of the principle of the DDoP filter. (a) The ideal DDoP kernel. (b) A derivative kernel in the Z direction. (c) An average smoothing kernel in X-Y plane. (c) The 3D rotation space of the DDoP filter, and (d) the discretization of this rotation space: the discretized directions, depicted with red dots, were predefined by the vertices of icosahedral [41] over a sphere.

ture and the intensity differences between the fissures and surrounding parenchyma, motivate us intuitively to design a filtering kernel with three parallel plates, which simultaneously probes the profile of a fissure patch and its neighboring background. This so-called directional derivative of plate (DDoP) filter with triple plates is illustrated in Fig. 2(b), and it is expected to give the highest response and record the corresponding direction when it detects a fissure.

3.1.1. Definition of the DDoP filter

Following the mathematical expression of the DoS filter, we use μ_{Up}, μ_{Mp} and μ_{Dp} to denote the mean intensity of the up, middle and down plate of the kernel. The derivative orthogonal to the plate is defined as

$$h_{DDoP} = \mu_{Mp} - \frac{1}{2}(\mu_{Up} + \mu_{Dp}). \tag{10}$$

From a perspective of modelling fissure's profile the DDoP kernel (Fig. 5(a)) can be decomposed into a derivative kernel in the Z direction (Fig. 5(b)) and an average smoothing kernel in X-Y plane (Fig. 5(c)), and a specified definition can be formulated as

$$h_z(z) = \begin{cases} 0, & \text{if } |z| \geq 3S \\ -\frac{1}{2}, & \text{if } S \leq |z| \leq 3S \\ 1, & \text{otherwise} \end{cases} \tag{11}$$

$$h_{xy}(x,y) = \begin{cases} 0, & \text{if } x^2 + y^2 \geq R^2 \\ 1, & \text{otherwise} \end{cases} \tag{12}$$

$$h(x,y,z) = h_{xy}(x,y) \cdot h_z(z), \tag{13}$$

where R determines the size of the average smoothing kernel, and S specifies the thickness of the fissure. We empirically set $R = 9$ and $S = 1.5$. A DDoP kernel with direction $\vec{n}$ is denoted with $h_{\vec{n}}$.

Generally, fissures detection can be performed by convolution of the rotated DDoP kernels $h_{\vec{n}}$ with the image I. A high response indicates the presence of a fissure feature and the direction of the corresponding kernel defines the normal orientation. Mathematically, the detection algorithm is defined as

$$\mathbf{r}^*(\mathbf{x}) = \max_{\vec{n}}(I(\mathbf{x}) * h_{\vec{n}}(\mathbf{x})), \tag{14}$$

$$\vec{\mathbf{n}}(\mathbf{x}) = arg\max_{\vec{n}}(I(\mathbf{x}) * h_{\vec{n}}(\mathbf{x})), \tag{15}$$

where $\mathbf{r}^*(\mathbf{x})$ is the magnitude of the fissure response, $\vec{\mathbf{n}}(\mathbf{x})$ its orientation at position $\mathbf{x} = (x,y,z)$ and $h_{\vec{n}}$ a rotated kernel with an azimuth angle φ and a polar angle θ, see Fig. 5(d). The range of φ and θ is $\varphi \in [0, 2\pi)$ and $\theta \in [0, \pi)$, respectively.

A common way to implement the rotating filter is to explicitly sample a bank of kernels, each of them representing a certain orientation. To ensure detection accuracy, we discretize the

rotation space into $N_o = 252$ directions according to [41], which are depicted with red dots in Fig. 5(e). Consequently, many convolutions are involved in the filter implementation and its computational complexity is $\mathcal{O}(N_o \times N \times R^3)$, where N is the number of voxels in the input image and R is the size of the kernel. Even if the convolution can be accomplished with a Fast Fourier Transform (FFT) algorithm, the complexity will be reduced only moderately to $\mathcal{O}(N_o \times N \times \log(N))$, while the memory consumption will be remarkably increased.

### 3.1.2. Accelerating with the spherical harmonics representation

To reduce the computational burden of the DDoP filter, we seek to decompose the original kernel $h_{\vec{n}}$ into a linear combination of basis kernels k_i that are independent of the rotation angle. In other words, these basis kernels can be used to synthesize the DDoP kernels of arbitrary orientations by the linear combinations of them. Due to the linearity and associativity of the convolution it is possible to construct the directional response $H_{\vec{n}}$ by the linear combination of individual responses K_i. This construction of directional responses only needs to convolute with basis filters once, which makes the DDoP filter efficient. We use a family of spherical harmonics [42] as basis kernels and determine the filter output as a function of orientation. In the following, we first introduce the spherical harmonic function and then present the reformulated DDoP filter in terms of spherical harmonics.

Spherical harmonic (SH) functions: Spherical harmonics are an orthogonal basis for representing functions defined on the surface of a sphere. They are the spherical analogue of the 1D Fourier series. Thus, any real-valued spherical function f can be expanded as a linear combination of the basis functions. For example,

$$f(\varphi, \theta) = \sum_{\ell=0}^{L} \sum_{m=-\ell}^{\ell} Y_m^\ell(\varphi, \theta) f_m^\ell \tag{16}$$

$$Y_m^\ell(\varphi, \theta) = \sqrt{\frac{(\ell-m)!}{(\ell+m)!}} P_m^\ell(cos(\theta)) e^{\mathbf{i}\varphi}, \tag{17}$$

where Y_m^ℓ is a spherical harmonic function, see Fig. 6, f_m^ℓ is an expansion coefficient, P_m^ℓ is a Legendre polynomial, ℓ and m denote the order and degree, respectively. For the ℓ-th order, there are $2\ell + 1$ SH basis functions, which are indexed in the range of $-\ell \leq m \leq \ell$. Similarly to a traceless Hessian matrix (symmetric) and a gradient (antisymmetric) function, the SH functions associated with an even order are symmetric; otherwise, they are antisymmetric. In a specific application, the finite frequency bands are used to approximate the target function $f(\varphi, \theta)$, and L denotes the cut-off frequency band. The rotation formula [43] of a spherical harmonic shows that a linear combination of spherical harmonics of order ℓ can synthesize an arbitrary rotation of any spherical harmonic Y_m^ℓ. Therefore, the spherical harmonics representation might provide an efficient way to calculate the DDoP filter responses.
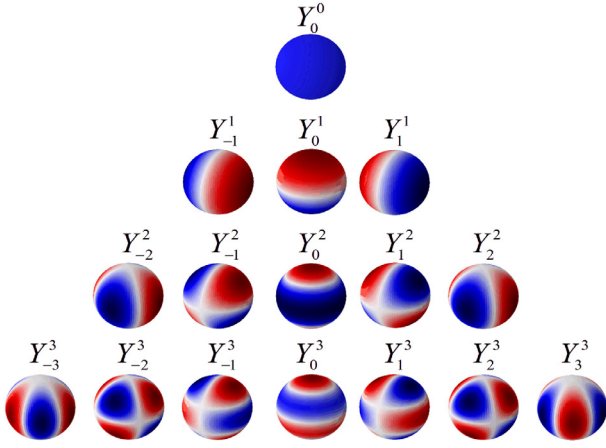
Fig. 6. Visual representations of the first few real-valued spherical harmonic basis functions Y_m^ℓ. Blue portions represent regions where the function is positive, and red portions represent where it is negative.

(a)

(b)   (c)   (d)

Fig. 7. Demonstration of the synthesized DDoP kernel based on the spherical Gaussian derivatives. (a) Image showing the center slices of the real-valued coefficient of spherical Gaussian derivatives $\nabla_0^\ell g_\sigma$, (b) the 3D rendering of the DDoP kernel, (c) the center slice of the DDoP kernel and (c) its surface representation.

Reformulating the DDoP filter: Reisert et al. [42] introduced the spherical derivatives that are just Gaussian-windowed solid harmonics and derived that the Gabor-like function can be written as a Taylor series in terms of these spherical derivatives. An excerpt of their deduction is given in Appendix A. Following this principle a DDoP kernel can be represented as

$$h_{\vec{n}}(\mathbf{x}) = \sum_{\ell=0}^{L_{max}} P(\ell) \mathbf{Y}^\ell(\vec{n}) \nabla^\ell g_\sigma(|\mathbf{x}|), \tag{18}$$

where g_σ is a Gaussian function with a scale of σ and $\mathbf{x} = (x, y, z)$ the spatial coordinate of voxels. In addition, $P(\ell)$ will control the shape of the filter kernel. Due to the axial and mirror symmetry of the DDoP kernel, it only has real-valued coefficients with even order. Thus, a group of appropriate $P(\ell)$ with $\ell = 0, 2, 4, \ldots$, integrating the even order spherical Gaussian derivatives, could be able to synthesize the DDoP kernel $h_{\vec{n}}$.

In this work, we select a scale of smoothing Gaussian $\sigma = 2$ and a cut-off frequency band $L_{max} = 8$ to construct the DDoP kernel. For completeness, the coefficients of spherical Gaussian derivatives with different orders $\ell = 0, 1, \ldots 9$ and degree $m = 0$ are depicted in Fig. 7(a). To obtain the parameters $P(\ell)$, we write the set of Eq. (18) as an over-determined linear system:
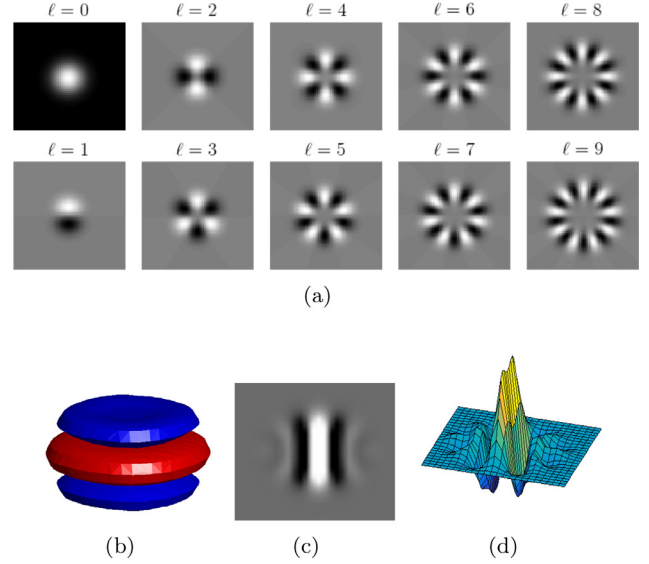
$$\mathbf{h} = GP,$$
$$G = [\nabla^0 g Y^0; \nabla^2 g Y^2; \nabla^4 g Y^4; \ldots; \nabla^{L_{max}} g Y^{L_{max}}],$$
$$P = [P(0), P(2), P(4), \ldots; P(L_{max})]. \tag{19}$$

The shape parameter P can be obtained by a straight-forward least-squared minimization. The shape of this synthesized kernel is shown in Fig. 7(b). Fig. 7(c) shows a center slice of the kernel, and Fig. 7(d) its surface representation. Observed from the shape of the approximate DDoP kernel, it is similar to an inverse second-order directional derivative of anisotropic Gaussian.

Consequently, the directional response of the DDoP filter $H_{\vec{n}}(\mathbf{x})$ is formulated as

$$H_{\vec{n}}(\mathbf{x}) = (h_{\vec{n}} * I)(\mathbf{x})$$
$$= \sum_{\ell=0}^{L_{max}} P(\ell) \mathbf{Y}^\ell(\vec{n}) \nabla^\ell (g_\sigma * I)(|\mathbf{x}|). \tag{20}$$

The workflow of this DDoP filtering is quite simple. First, a Gaussian of width σ is applied to the 3D image. Then, the Gaussian spherical derivatives are calculated with a finite difference scheme [42]. Finally, the responses are generated from the inner products between the Gaussian spherical derivatives and spherical

harmonics. Thus, the DDoP filtering requires only one initial convolution with complexity $\mathcal{O}(N \log N)$. The complexity of spherical Gaussian derivatives $\nabla^\ell(g_\sigma * I)(|\mathbf{x}|)$ is in $\mathcal{O}(NL_{max}^2)$ [42] and the remaining inner products is in $\mathcal{O}(N)$ with a small constant. The efficiency of the DDoP filtering is largely improved. As an example, a slice from a pulmonary CT scan and its filtered results are illustrated in Fig. 3(f).

3.2. Post-processing pipeline for fissure segmentation

After filtering the CT image with the proposed DDoP method, the pulmonary fissures and other plate-like structures are efficiently enhanced. Nevertheless, due to the various image contrast, the high curvature fissures and the adjacent clutter, the responses of fissures are not consistent, which makes a simple threshold segmentation unfeasible. Here, we present a simple two-stage post-processing scheme to extract fissures in the filtered images. First, inspired by the fact that adjacent fissure voxels usually have similar normal directions but its adjacent interference deviates saliently, we present an orientation partition denoising and merging algorithm to eliminate the non-fissure structures. Then, based on the connectivity of the pulmonary fissures, a region growing method is used to reconstruct the missing fissures due to its high curvature, for the high curvature fissures are occasionally eliminated in the previous denoising stage. The detailed algorithms are described as follows.

3.2.1. Orientation partition based denoising and merging

To isolate the lung fissures from other objects, we use the information that normal fissures have large connected regions and the variation of their normal orientations is relatively minor among plate-like structures. We employed a partition and merging strategy (Algorithm 1) to extract the coarse fissures and its schematic illustration is shown in Fig. 8.

Firstly, according to the predefined orientations over a sphere shown in Fig. 5(e), we iteratively extracted fissure-like objects which belong to each orientation by comparing the predefined orientation with the normal of fissures. For a demonstration, fissure-like structures from two orientations are illustrated in Fig. 8(a) and Fig. 8(c), respectively. Secondly, we used a connected component

Algorithm 1 The orientation partition denoising and merging algorithm

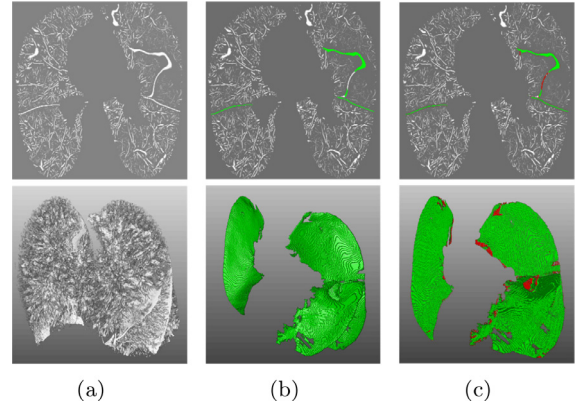**Input:** M_{ridge}: Magnitude; $\vec{O}$: Normal orientation; $\vec{n}$: Predefined partition directions

Output: F_{coarse}

1: $F_{thr} = \begin{cases} M_{ridge}, if M_{ridge} > th, \\ 0, otherwise. \end{cases}$

2: $\vec{O}^* = \vec{O} \cdot F_{thr}; \vec{O}^* = \frac{\vec{O}^*}{|\vec{O}^*|}$

3: $F_{acc} = \Phi$: initialize the accumulated labelling fissures

4: **for** each predefined direction $\vec{n}_i$ **do**

5:     $F_{n_i}^* = \begin{cases} 1, if \ (\vec{n}_i \cdot \vec{O}^*) > 0.98, \\ 0, otherwise. \end{cases}$

6:     remove isolated noise that is less than T voxels in size and obtain F_{label}

7:     $F_{acc} = F_{acc} \bigcup F_{label}$

8: **end for**

9: Given three types of fissures in left and right lungs, we empirically select the three largest connect components which at least contain 10000 voxels from F_{acc} as the F_{coarse}

10: return F_{coarse}

filter, the area opening method [44], to remove the isolate noise, see Fig. 8(b) and Fig. 8(d). Then, for each orientation, the denoised fissures are merged into the accumulated fissures F_{acc} (Fig. 8(e)). Finally, since the fissures should appear as large connected components, a connected component containing less than 10000 voxels is discarded, and the remaining three largest connected components in the F_{acc} are selected as the initial fissure segmentation result F_{coarse} (Fig. 8(f)).

3.2.2. Region growing to reconstruct fissures

As shown in Fig. 9(b), in the previous denoising step, some locally high curvature fissures are occasionally missed due to their seriously variable normal orientations. As a compensation for this weakness, a region growing approach is applied to reconstruct the fissures. The under-segmented fissures F_{coarse} from the previous step are used as seeds and the binarized result of magnitude responses of fissures are used as a mask which contains the con-

Fig. 8. Demonstration of orientation partition denoising and merging. (a) The fissures from orientation O_i. (b) The denoised fissures from orientation O_i. (c) The fissures from orientation O_j. (d) The denoised fissures from orientation O_j. (e) The merged fissures. (f) The segmentation from connected component analysis.

Fig. 9. Visualization of 2D (the first row) and 3D images (the second row) of the segmented fissures in post-processing stages. The segmented fissures are rendered in green, and the added fissures obtained in region growing are rendered in red. (a) The magnitude result of the DDoP filter; (b) the denoising and merging result; and (c) the complete fissures reconstructed from the multi-seeded region growing step.

straints of fissures growing. For computational simplicity and noise suppression, we reconstructed the fissure lines from the sagittal slice by slice using the binary image reconstruction algorithm [45]. As shown in Fig. 9(c), the missing fissures in Fig. 9(b) are recovered through the region growing method.

4. Experiments and evaluation

In this section, the proposed DDoP filter and segmentation algorithm are validated with two public datasets: VIA-ELCAP and LOLA11 (see Section 4.1). The proposed algorithms were developed with hybrid programming of Matlab and C++ on the basis of the Spherical Tensor Algebra (STA) toolkit [46]. Mevislab [47] was used for visualizing the 3D results. The configuration of the computer was a 2.10 GHz 8 cores CPU, 64 GB RAM, and an Ubuntu 16.04 LTS operating system.

4.1. Dataset and reference

For demonstration and evaluation, we used low-dose non-contrast enhanced chest CT images from the VIA-ELCAP image database [48,49] and the public dataset from the LObe and Lung Analysis 2011 (LOLA11) challenge [50]. The VIA-ELCAP database currently consists of 50 low-dose whole-lung CT scans of lung cancer patients. These CT scans were obtained in a single breath hold with a 1.25 mm slice thickness. These were used to verify the feasibility of our method for low-dose CT scans.

The LOLA11 dataset consists of 55 chest CT scans originating from different hospitals with various pathology and abnormalities. The transverse resolution ranged from 0.53 mm and 0.78 mm whilst the slice thickness was between 0.3 mm and 1.5 mm. Visible-only fissures were sparsely marked on nine coronal slices in the LOLA11 dataset [36], which were used as the ground truth in our quantitative evaluation. For qualitative evaluation, ground-truth data was obtained by a radiologist, who manually delineated the boundaries between lung lobes using the Chest Imaging Platform [51] in the 3D Slicer environment. The user was asked to mark a small number of points on each fissure. Those points were then interpolated or extrapolated to form complete boundaries between lobes. The labeled boundaries are rendered in red in Fig. 11.
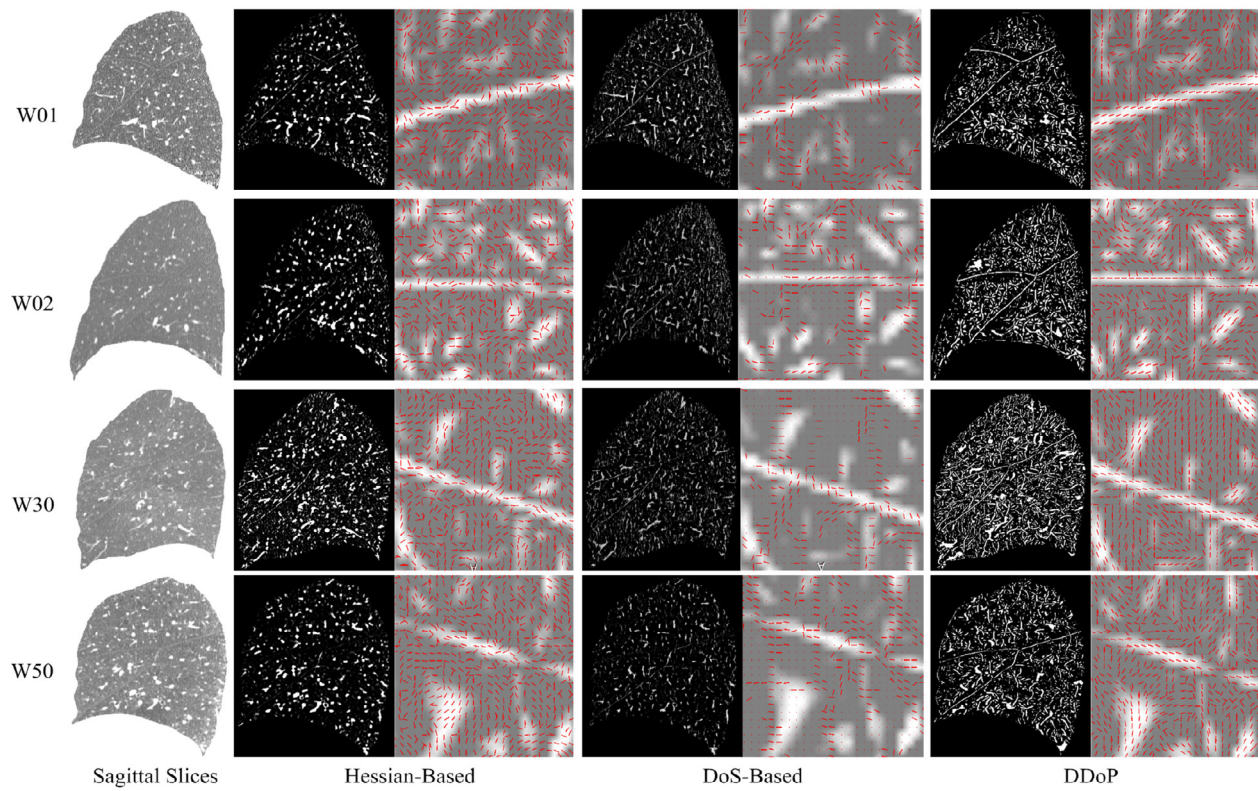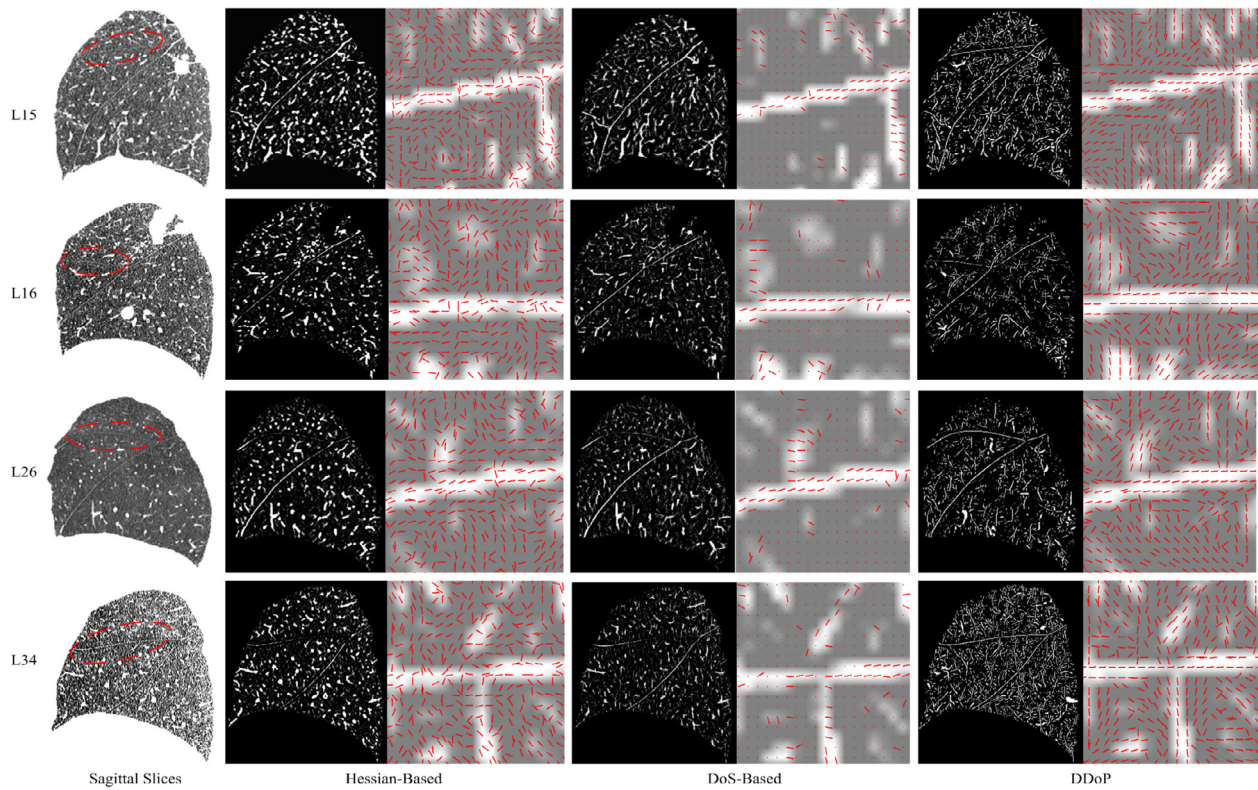
4.2. Qualitative evaluation and comparison

The qualitative evaluation was performed on the challenging CT scans to show the capability of the enhancement and segmentation algorithms. Furthermore, a set of low-dose CT scans was used
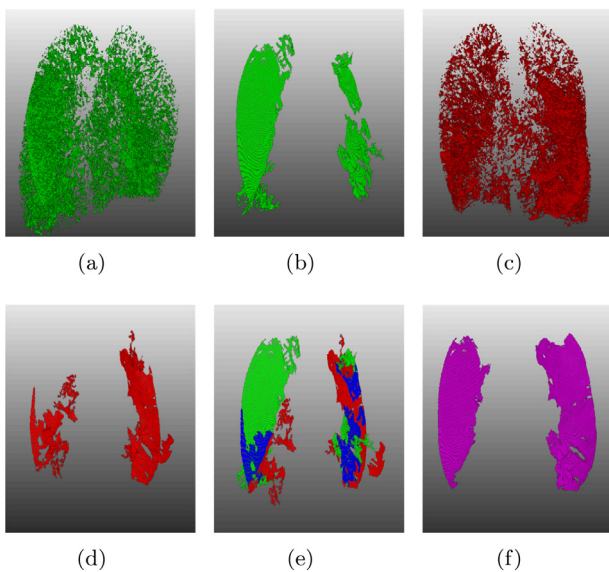
Fig. 10. Representative enhancement results: (a) four LOLA11 scans (case15, case16, case26 and case34) and (b) four lung cancer scans (case01, case02, case30 and case50). The magnitude responses and orientation fields obtained from different methods. From left to right, it depicts the original sagittal slices, Hessian-based, DoS-based and DDoP filtering results. Note that the normal orientations from the Hessian and the DDoP are rotated by 90 degrees.
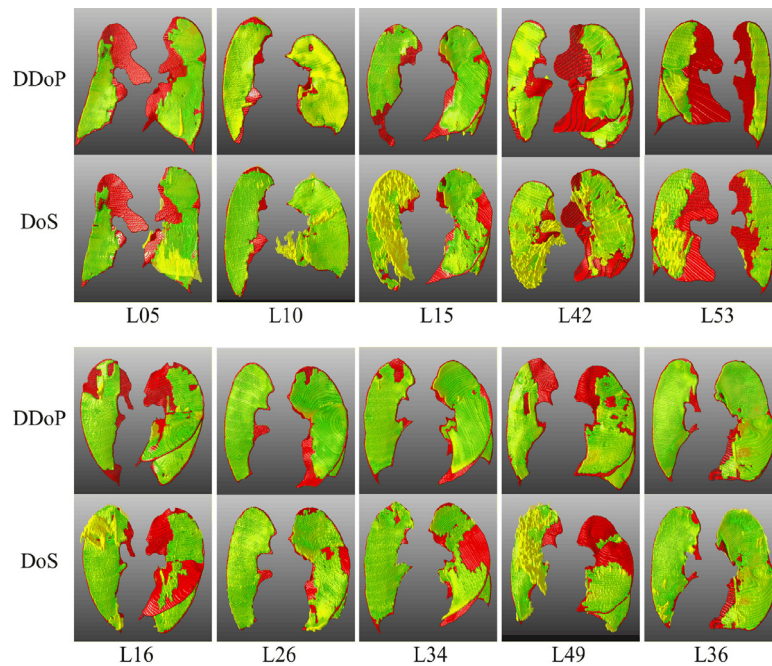
Fig. 11. Demonstration of fissure segmentations on LOLA11 dataset. The segmented fissures obtained from the DDoP and DoS approach are rendered in yellow, the manual interlobar boundary reference in red and the overlapping regions in green.

to verify the adaptability of the proposed method. Here, we only qualitatively evaluated the performance with some representative data.

Representative fissure enhancement results are displayed in Fig. 10 (a) for the LOLA11 dataset and Fig. 10 (b) for the lung cancer dataset (VIA-ELCAP). The Hessian-based and DoS-based methods were used for comparison. A single scale $\sigma = 1$ voxel was used for Hessian-based method and its three parameters (α, β, γ) were set to (0.5,0.5,500). For the DoS-based filters, we adopted the same parameters as the original paper [36], i.e. $L = 11, S = 3, k = 0.7$. Due to both the magnitude response and the orientation information contributing to fissures segmentation in our framework, they will be analyzed and illustrated respectively in a comparative way.

As observed, both the Hessian-based and DoS-based filters suffered much from missing detection and lack of consistent orientation on the weak fissures. That is because both of them have an intrinsic limitation for describing the extremely anisotropic thin fissures due to the limited contextual information. As pointed out by Klinder et al. [25], Hessian-based filters work too locally, so it is highly sensitive to image noise. Although the sticks of the DoS-based filter have large anisotropy within slices, the inter-slice information is ignored. Therefore, these two types of methods have difficulties to detect point-cloud-like or inhomogeneous fissures. The proposed DDoP filter is a 3D plate detector with a large anisotropic context, which has the ability to cope with weak point-cloud-like fissures. As shown in Fig. 10, weak fissures are clearly enhanced and their consistent orientations are obtained by the DDoP filter, which can benefit subsequent segmentation of fissures.

To verify the segmentation performance of the proposed framework and provide a global impression, 10 CT scans were chosen from the LOLA11 dataset for visual inspection. In Fig. 11, the fissure segmentation results of the DoS method and our proposed framework are illustrated in pairs. The extracted fissures are rendered in yellow, the references in red and their overlapped region in green. Therefore, the yellow and red regions can be interpreted as over-segmentations (false detections) and under-segmentations (missing detections), respectively.

As illustrated in the first five pairs of 3D visualization of segmented fissures in Fig. 11, our method hardly suffers from over-segmentations because of the large anisotropic context and post-processing with the 3D orientation partitioning. Conversely, due to the lack of inter-slice information, the DoS method is sensitive to adhering noise and thus generates some false detections. Especially, these over-segmentations can be clearly seen on pathological examples denoted with L15, L42, and L53. On the another hand, the last five pairs of segmented fissures, shown in Fig. 11, indicate that the DoS method has limitations on segmenting weak fissures as the authors of [37] have alleged to. For the DoS method, the horizontal fissures are prone to under-segmentations, as their orientation are often parallel to the axial imaging plane, potentially obscuring the fissures in CT scans, as illustrated in L16, L34, and L49.

However, as an extended version of the DoS-based method, our framework which combines the real 3D plate detector (DDoP) with the partition denoising and region growing algorithms has the ability to cope with the deteriorated CT images for the segmentation of fissures. Therefore, even with challenging lung CT scans like extensive deformations in the lungs, focal regions of emphysema, bullous lung disease and fibrosis, our presented algorithm can still achieve a robust and accurate segmentation on the visible fissures.

In addition to the LOLA11 dataset, the VIA-ELCAP dataset was used to verify the feasibility of our algorithm applying on low-dose lung cancer CT images. We randomly selected nine CT scans from this low-dose dataset for the experiment. Because low doses are required for CT images for mass screening, the quality of the images is inferior to normal-dose CT scans. Due to the low image quality and high noise levels, the DoS method could not produce satisfying results. Therefore, only the segmentation results of our method are illustrated in Fig. 12. Although some holes exist in segmented fissures, the main inter-lobular borders are still clearly visible.

To demonstrate the contribution of the DDoP filter and the proposed post-processing approach, we compared the segmentation results before and after post-processing for each method (Hessian,
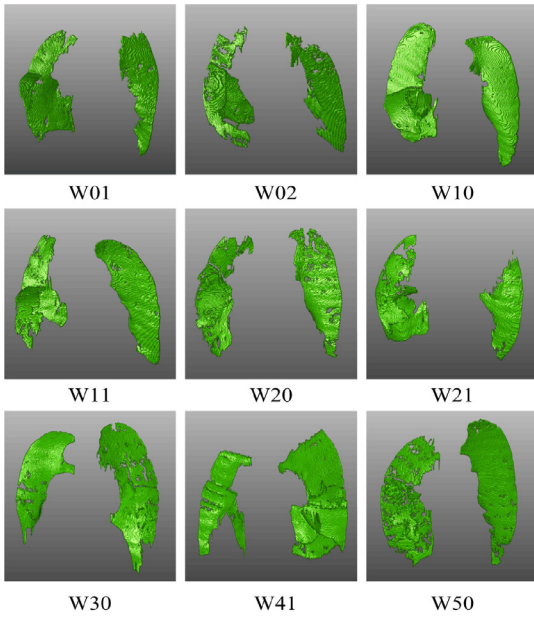
Fig. 12. Illustration of fissure segmentations on the VIA-ELCAP dataset by the DDoP method.

DoS, Zero-order, DDoAG and DDoP methods) in Fig. 13, where the output of each filter was thresholded at an optimal threshold. This comparison shows that the contribution of the post-processing approach is to reduce false positives on the basis of enhancement results.

4.3. Quantitative evaluation

The quantitative evaluation is based on a definition of points on the fissures as True Positive (TP), False Positive (FP) or False Negative (FN). This definition is based on a correspondence between the points of the reference and the points of the fissures to be evaluated. A point on the segmented fissures is marked as TP_1 if there is at least one point on the reference at a distance less than 3 mm or otherwise FP. A point of the reference is marked as TP_2 if the distance to at least one point on the evaluated fissures is less than 3 mm or otherwise FN. TP, FP, and FN are defined on the entire annotated slice.

The Precision and Recall are defined as $\frac{TP_1}{TP_1+FP}$ and $\frac{TP_2}{TP_2+FN}$, respectively. The $F_1 - score$, which is defined as $\frac{2 \cdot \text{Precision} \cdot \text{Recall}}{\text{Precision} + \text{Recall}}$, was used in our evaluation. It represents the ability to extract the visible fissures. To distinguish the over- and under-segmentation errors, we used a False Detection Rate (FDR = FP/(TP_1 + FP)) and a False Negative Rate (FNR = FN/(TP_2+FN)) as quantitative indices.
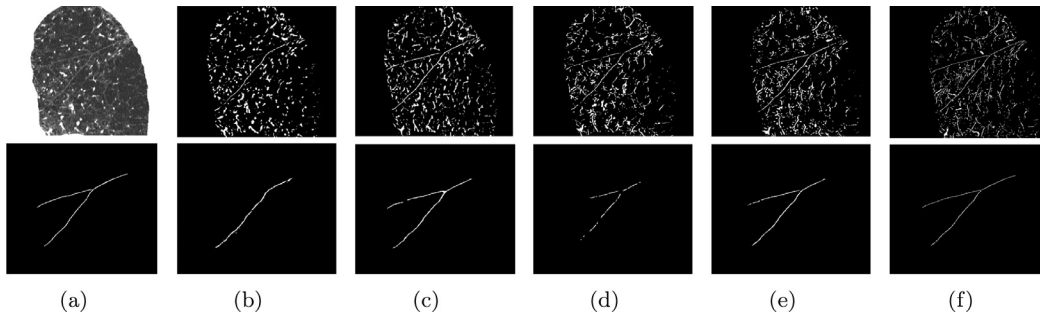
We quantitatively compared DDoP against Zero-Order, Hessian, DoS and DDoAG methods before and after post-processing on the LOLA11 dataset in Fig. 14. We used paired t-test to test the significance of the differences in performance between approaches with regards to evaluation indices. Significant differences ($p < .005$) are marked with stars in Fig. 14.

To conduct quantitative evaluation before post processing, we binarized the magnitude responses of these filters with an optimal threshold. Fig. 14(a) shows that both DDoP and DDoAG have a significantly lower FNR compared to DoS and Hessian ($p < .005$) before post-processing on the LOLA11 dataset. Due to the lack of post-processing for removing false positives, all methods have a similarly high FDR and low $F1 - score$.

For a fair comparison after post processing, all methods were configured with the same post processing algorithm. Fig. 14(b) shows that DDoP has a significantly lower FDR compared to DoS ($p < .005$), a significantly lower FNR compared to Zero-Order and Hessian ($p < .005$), and thus a significantly greater $F1 - score$ compared to Zero-Order, Hessian and DoS ($p < .005$). Due to the similar filtering kernel, DDoAG and DDoP have a similar performance. Furthermore, the FDR for each method is greatly decreased after post processing.

Table 1 shows the overall median and mean indices for all methods after post-processing on the LOLA11 dataset. DDoP has the highest detection accuracy in terms of $F1 - score$, DDoAG has the lowest FDR, and DoS has the lowest FNR. Due to the asymmetrical kernel, DoS may be more robust than DDoP to abnormal fissures whose profile might take a step shape or appear as a thickened band arising from adjacent vascular tissues. Although DoS has a slightly lower FNR compared to DDoP, it has a higher FDR on the LOLA11 dataset.

4.4. Parameter configuration

For the DDoP filter, there are two parameters including the cutoff frequency band L and the scale of Gaussian kernel σ, that need to be configured. We empirically fixed $\sigma = 2$ to determine the inter-plate spacing $2S \doteq 3$ according to the thickness of fissures in the clinical images.

The parameter L should be chosen to control the suppression of noise while accommodating the local curvature of a fissure. To verify its influence on the fissure segmentation, we calculate the $F_1 - score$ on a part of LOLA11 segmentations from our proposed method using a range of values for L. As shown in Fig. 15, there was a noticeable increase in the median of $F_1 - score$ value from $L = 2$ to $L = 8$ and the maximum locating at $L = 8$. The $F_1 - score$ at $L = 10$ is slightly lower than $L = 8$. This means that a plateness filter with a higher order can achieve a higher detection accuracy within the tolerance of fissures' curvature. Therefore, we set $L = 8$.

There are also several parameters in the post-processing steps. The area opening parameter T is empirically selected to 600 voxels.

| (a) | (b) | (c) | (d) | (e) | (f) |

Fig. 13. Comparison of the contribution of filters and post-processing. (a) CT sagittal slice (top) and ground truth (bottom), (b)-(f) denotes the results of filters (top) and post-processing (bottom) from the Hessian, DoS, Zero-order plateness, DDoAG and DDoP filter, respectively.

Table 1
Comparison of quantitative indices for five methods after post-processing on 55 cases from LOLA11.

Type	$F_1 - score$		FDR		FNR	
	Mean	Median	Mean	Median	Mean	Median
Zero-Order	0.668 ± 0.253	0.753	0.200 ± 0.225	0.142	0.317 ± 0.298	0.162
Hessian	0.747 ± 0.239	0.843	0.105 ± 0.114	0.082	0.309 ± 0.258	0.226
DoS	0.781 ± 0.165	0.848	0.262 ± 0.144	0.215	$\mathbf{0.120 \pm 0.184}$	**0.058**
DDoAG	0.857 ± 0.098	0.891	$\mathbf{0.091 \pm 0.075}$	**0.078**	0.180 ± 0.132	0.138
DDoP	$\mathbf{0.858 \pm 0.103}$	**0.899**	0.116 ± 0.079	0.095	0.163 ± 0.132	0.106
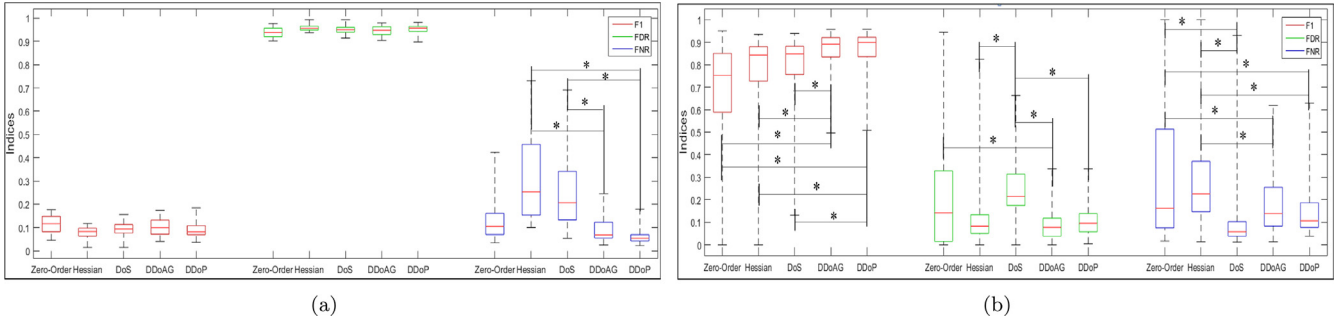
Fig. 14. Comparison of quantitative indices ($F_1 - score$, FDR and FNR) for Zero-Order, Hessian-based, DoS-based, DDoAG and DDoP methods on the LOLA11 dataset. The significant differences ($p < .005$) between approaches are marked with stars. (a) Evaluation before post-processing, and (b) after post-processing.
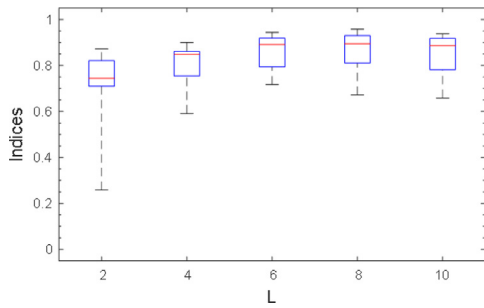
Fig. 15. Box plots of our fissure segmentation with different frequency cut-off band L on a part of the LOLA11 dataset. The medians of the boxplots are 0.744, 0.848, 0.891, 0.895, 0.887 for $L = 2, 4, 6, 8, 10$.

For the connected component analysis, the three largest connected components containing at least 10000 voxels are selected.

4.5. Comparison of running time for different methods

With respect to the computation efficiency, the runtime of each method for a typical $512 \times 512 \times 400$ size image is reported in Table 2. The Hessian method is the most efficient as it uses a small isotropic kernel. As the 3D matched filters, the zero-order and DDoAG filters have similar efficiency. They are slower than other methods as they need to calculate the matching results in a large number of directions in 3D space. Since the DoS filter is a simplified filter, it is approximately 4 times faster than the zero-order and DDoAG methods. With the acceleration of the spherical harmonics, the DDoP method is approximately 9 times faster than the zero-order and DDoAG methods.

Table 2
Comparison of the runtime for five methods.

Method	Zero-order	Hessian	DoS	DDoAG	DDoP
Time (s)	7793	435	1890	7816	850

5. Discussion

The original DoS filter has a limitation in detecting weak and point-cloud like fissures, due to its limited context and homogeneous intensity assumption. To overcome this limitation we extended the DoS filter to a DDoP filter which uses more contextual information and avoids the requirement of homogeneous intensity constraint. For computational efficiency, the DDoP filter was implemented in a spherical tensor derivative framework. Additionally, a post-processing framework based on the coherence of a fissure's normal orientation was proposed to segment fissures.

Using a set of chest CT scans especially with point-cloud-like fissures and a low-dose dataset, the validation experiments were conducted in a comparative way. It was verified that the proposed algorithm outperformed the conventional Hessian-based filters and DoS-based detectors in both accuracy and robustness to noise due to a larger context and a higher anisotropy. Particularly, our method can cope with challenging data like low-dose CT scans. This was verified not only from the visual inspection of qualitative experiments but also with quantitative indices. As shown in Fig. 11, the missing detections and false detections in our approach are less than in the DoS approach. Furthermore, the mean $F_1 - score$ of our method was higher than the DoS and Hessian-based methods, and the variance of $F_1 - score$ was lower than both of them, which indicates that our approach achieves higher segmentation accuracy and is more robust to noise.

Unlike the 2D approaches, the proposed DDoP filter, which is a 3D filter, directly detects fissures in a 3D image. The DDoP filter takes the 3D appearance of a fissure into account and thus can distinguish a fissure from other structures that would appear similar on slices. Because of providing 3D context, the DDoP filter has a stronger noise suppression ability than the 2D filter. The 3D filter would consume more computational resources than the 2D filter. The DDoP filter was implemented in the spherical derivative framework, which can alleviate this problem.

The piecewise plane-fitting algorithm presented in [28], probing the existence of a plate with the assumption that a fissure has a low curvature in a local volume, is similar to the DDoP filter since both of them directly detect the plate or plane in a 3D space with the same assumption. However, the underlying filtering

kernel of this plane-fitting method is a zero-order plateness kernel, while our proposed method is a second-order plateness kernel. They use different information to detect plates. The former uses the intensity character of fissures, while the latter uses the contrast between fissures and background. Furthermore, the piecewise plane-fitting method was implemented in an optimization framework. Therefore, it is essentially different from the DDoP filter from the filtering and implementational perspective.

The inverse directional derivative of 3D anisotropic Gaussian (DDoAG) kernel resembles the DDoP kernel very much. They almost have the same anisotropy. However, as mentioned in Section 2.3 and 4.5, the computation of the explicit dense matching in a 3D space is costly. Thus, it is impractical to apply the DDoAG filter to detect fissures.

The primary limitation of the proposed framework is handling with severe pathological cases whose fissures are disconnected. Since the post-processing procedure is based on the assumption that fissures are flat and connected, the disconnected or high curvature fissures may be eliminated as noise. The region growing can recover some high curvature fissures, which is good for accessing fissure integrity. However, the region growing is sensitive to the threshold parameter. An inappropriate threshold may lead to under-segmentation or over-segmentation and thus may disturb the fissure integrity measure. The FissureNet method using global context dose not require post-processing and therefore can be directly used to access the fissure integrity. From this perspective, the FissureNet is better than the proposed method. Although our method was designed to segment visible fissures, we should claim that the fissure surface interpolation and extension will be applied if our goal is to segment lung lobes in the future.

As a convolutional neural network (CNN), FissureNet achieved a promising performance on fissures segmentation [8]. The overall PR-AUC for FissureNet on the COPDGene and lung cancer dataset was 0.980 and 0.966, respectively. Recently, it has been extended to a LobeNet [9], which obtains 0.9178 in Lobe Score[1] on the LOLA11 dataset. A drawback of deep learning methods is the requirement of a large training dataset with manual segmentations and a large computation resource for training the network. However, this effort needs to be done only once. Although CNNs are capable of learning features directly from the original data, if we would provide the CNN both the original image and the filtered image obtained from the DDoP filter, it may improve the performance of CNNs further. Thus, adding "image processing knowledge" or "domain knowledge" to CNNs is our future work.

6. Conclusion

In this paper, we presented a framework to enhance and segment lung fissures on the basis of a novel plate detection algorithm in the 3D space. The accuracy and robustness of fissures segmentation were improved by applying a real 3D plate detector, an orientation partition denoising and a region growing algorithm. A significant advantage of the proposed plate detector is that it has a sufficiently large context and can efficiently detect weak fissures because of its spherical harmonics representation. The coherence of the normal direction and the connectivity of the lung fissure were well utilized in the post-processing procedure, which contributes to the accuracy and robustness of segmenting fissures.

Declaration of Competing Interest

The authors declare that they have no known competing financial interests or personal relationships that could have appeared to influence the work reported in this paper.

---

[1] https://lola11.grand-challenge.org/evaluation/results/.

CRediT authorship contribution statement

Hong Zhao: Conceptualization, Methodology, Software, Validation, Writing - original draft. **Berend C. Stoel:** Investigation, Writing - review & editing. **Marius Staring:** Investigation, Writing - review & editing. **M. Bakker:** Data curation. **Jan Stolk:** Data curation. **Ping Zhou:** Visualization. **Changyan Xiao:** Funding acquisition, Writing - review & editing, Conceptualization.

Acknowlgedgments

Appendix A. Spherical harmonics representation related theory

According to Reisert et al [42], a filter kernel can be represented in terms of spherical Gaussian derivatives. In this section, we summarized the deduction of this spherical harmonics representation from [42].

The expansion of a plane wave in spherical harmonics is

$$
\begin{aligned}
e^{\mathbf{ik}^\top \mathbf{r}} &= \sum_\ell (2\ell+1)(\mathbf{i})^\ell j_\ell(kr) P_\ell\left(\frac{\mathbf{k}^\top \mathbf{r}}{kr}\right) \\
&= \sum_\ell (2\ell+1)(\mathbf{i})^\ell j_\ell(kr) \mathbf{Y}^\ell(\mathbf{r}) \bullet_0 \mathbf{Y}^\ell(\mathbf{k}),
\end{aligned} \tag{A.1}
$$

where j_ℓ is the spherical Bessel function and P_ℓ is a Legendre polynomial. $\bullet_\ell$ denotes spherical tensor coupling, and here, $\bullet_0$ is equivalent to the inner product. This formulation can be rewritten in terms of solid harmonics as follows

$$
e^{\mathbf{ik}^\top \mathbf{r}} = \sum_{n \geq i} (\mathbf{i})^{n+i} \alpha_{n,i} \mathbf{R}_i^n(\mathbf{r}) \bullet_0 \mathbf{R}_i^n(\mathbf{k}), \tag{A.2}
$$

where

$$
\alpha_{n,i} = \frac{(2(n-i)+1)}{i! 2^i (2n+1)!!} = \frac{(2(n-i)+1)}{i! 2^i (2n+1)(2n-1)(2n-3)\ldots}. \tag{A.3}
$$

The solid harmonic is defined as $\mathbf{R}_i^n(\mathbf{r}) := r^{n+i} \mathbf{Y}^{n-i}(r)$. According to the Fourier shift properties, the above expression can be used to define a shift by means of a spherical expansion. Consider a function $\tilde{f}(\mathbf{k})$ in Fourier domain and multiply it by $e^{\mathbf{ik}^\top \mathbf{t}}$, i.e. shift the function $f(\mathbf{k})$ in the spatial domain.

$$
\begin{aligned}
e^{\mathbf{ik}^\top \mathbf{t}} \tilde{f}(\mathbf{k}) &= \sum_{n \geq i} \alpha_{n,i} \mathbf{R}_i^n(\mathbf{t}) \bullet_0 ((\mathbf{i})^{n+i} \mathbf{R}_i^n(\mathbf{k}) \tilde{f}(\mathbf{k})) \\
&= \sum_{n \geq i} \alpha_{n,i} \mathbf{R}_i^n(\mathbf{t}) \bullet_0 (\tilde{\nabla}_i^n \tilde{f}(\mathbf{k})).
\end{aligned} \tag{A.4}
$$

To get from the first to second line in the above expression we need the Fourier transform of multiple spherical derivatives, i.e. $(\tilde{\nabla}_i^n \tilde{f})(\mathbf{k}) = (\mathbf{i})^{n+i} \mathbf{R}_i^n(\mathbf{k}) \tilde{f}(\mathbf{k})$. The detailed proof is given in [42]. Based on Fourier transform properties, formula (A.4) can be transferred to the spatial domain and expressed as

$$
(\tau_\mathbf{t} f)(\mathbf{r}) = f(\mathbf{r}+\mathbf{t}) = \sum_{n \geq i} \alpha_{n,i} \mathbf{R}_i^n(\mathbf{t}) \bullet_0 (\nabla_i^n f(\mathbf{r})), \tag{A.5}
$$

which can be interpreted as a Taylor series written in spherical derivatives.

We can use a pure imaginary shift to generate a Gabor function from a Gaussian. For example, shifting $g(\mathbf{r}) = e^{\frac{-\mathbf{r}^\top \mathbf{r}}{2}}$ by $\mathbf{ik}$ generates this Gabor function

$$
\begin{aligned}
G_\mathbf{k}(\mathbf{r}) &= e^{\frac{-(\mathbf{r}+\mathbf{ik})^\top (\mathbf{r}+\mathbf{ik})}{2}} \\
&= g(\mathbf{r}) e^{-\mathbf{ik}^\top \mathbf{r}} e^{-\mathbf{k}^\top \mathbf{k}/2} \\
&= g(\mathbf{r}) e^{-\mathbf{ik}^\top \mathbf{r}} g(\mathbf{ik})
\end{aligned} \tag{A.6}
$$

where $G_{\mathbf{k}}$ is a spherical Gabor function with wave frequency $-\mathbf{k}$. The magnitude of frequency is $|\mathbf{k}| = k$, and whose direction is $\mathbf{n} = \mathbf{k}/k$.

Thus, a convolution with a Gabor function is equivalent to a convolution with a Gaussian and then performing a shift.

$$G_{\mathbf{k}} * f = (\tau_{\mathbf{ik}} g) * f = \tau_{\mathbf{ik}}(g * f) = \tau_{\mathbf{ik}} f_\sigma \tag{A.7}$$

This shift can be written as:

$$(\tau_{\mathbf{ik}} f_\sigma)(\mathbf{r}) = \sum_{n \geq i} (\mathbf{i})^{n+i} \alpha_{n,i} \mathbf{R}_i^n(\mathbf{k}) \bullet_0 (\nabla_i^n f_\sigma(\mathbf{r})) \tag{A.8}$$

From a computational perspective we have to compute the smooth derivative images $\nabla_i^n f_\sigma$ and collect those with the same tensor rank in one sum. The above formula can be rewritten as

$$G_{\mathbf{k}} * f = \sum_{n-i=\ell} (\mathbf{i})^{n-i}(\mathbf{i})^{2i} \alpha_{n,i}(k)^{n+i} \mathbf{Y}^{n-i}(\mathbf{k}) \bullet_0 (\nabla_i^n f_\sigma(\mathbf{r}))$$
$$= \sum_{n-i=\ell} (\mathbf{i})^{n-i}(-1)^i \alpha_{n,i}(k)^{n+i} \mathbf{Y}^{n-i}(\mathbf{k}) \bullet_0 (\nabla_i^n f_\sigma(\mathbf{r})) \tag{A.9}$$

Let

$$\mathbf{A}^\ell = \sum_{n-i=\ell} (-1)^i \alpha_{n,i}(k)^{n+i} \nabla_i^n f_\sigma(\mathbf{r}) \tag{A.10}$$

then

$$G_{\mathbf{k}} * f = \sum_\ell (\mathbf{i})^\ell \mathbf{Y}^\ell(\mathbf{k}) \bullet_0 \mathbf{A}^\ell \tag{A.11}$$

To compute the response of the Gabor filter in a specific direction, we just need to select the direction of $\mathbf{k}$ and compute $\sum_\ell (\mathbf{i})^\ell \mathbf{Y}^\ell(\mathbf{k}) \bullet_0 \mathbf{A}^\ell$. It would become even more efficient if we restrict the computation of ∇_i^n to a certain subset, e.g. let $i = 0$. Eq. (A.10) is transformed to the following equation with $i = 0$.

$$\mathbf{A}^\ell = \sum_{n-0=\ell} (-1)^0 \alpha_{n,0}(k)^{n+0} \nabla_0^n f_\sigma(\mathbf{r})$$
$$= \frac{(k)^\ell}{(2\ell-1)!!} \nabla^\ell f_\sigma \tag{A.12}$$

where $(2\ell-1)!! = (2\ell-1)(2\ell-3)(2\ell-5)\ldots$, and $f_\sigma = g * f$. Known from the above derivation, the computationally most expensive part is the computation of $\mathbf{A}^\ell$, namely the spherical derivatives. The implementation of spherical derivatives proposed in [42,46] is used in our application.

References

[1] A. Aziz, K. Ashizawa, K. Nagaoki, K. Hayashi, High resolution CT anatomy of the pulmonary fissures, Journal of thoracic imaging 19 (3) (2004) 186–191.
[2] P. Cronin, B.H. Gross, A.M. Kelly, S. Patel, E.A. Kazerooni, R.C. Carlos, Normal and accessory fissures of the lung: evaluation with contiguous volumetric thin-section multidetector CT, European journal of radiology 75 (2) (2010) e1–e8.
[3] T. Doel, D.J. Gavaghan, V. Grau, Review of automatic pulmonary lobe segmentation methods from CT, Computerized Medical Imaging and Graphics 40 (2015) 13–29.
[4] J. Padgett, A.M. Biancardi, C.I. Henschke, D. Yankelevitz, A.P. Reeves, Local noise estimation in low-dose chest CT images, International journal of computer assisted radiology and surgery 9 (2) (2014) 221–229.
[5] E.M. van Rikxoort, B. van Ginneken, M. Klik, M. Prokop, Supervised enhancement filters: application to fissure detection in chest CT scans, IEEE transactions on medical imaging 27 (1) (2008) 1–10.
[6] Q. Wei, Y. Hu, J.H. MacGregor, G. Gelfand, Automatic recognition of major fissures in human lungs, International journal of computer assisted radiology and surgery 7 (1) (2012) 111–123.
[7] K. George, A.P. Harrison, D. Jin, Z. Xu, D.J. Mollura, Pathological pulmonary lobe segmentation from CT images using progressive holistically nested neural networks and random walker, in: Deep Learning in Medical Image Analysis and Multimodal Learning for Clinical Decision Support, Springer, 2017, pp. 195–203.
[8] S.E. Gerard, T.J. Patton, G.E. Christensen, J.E. Bayouth, J.M. Reinhardt, FissureNet: A deep learning approach for pulmonary fissure detection in CT images, IEEE Transactions on Medical Imaging 38 (1) (2019) 156–166.
[9] S.E. Gerard, J.M. Reinhardt, Pulmonary lobe segmentation using a sequence of convolutional neural networks for marginal learning, in: 2019 IEEE 16th International Symposium on Biomedical Imaging (ISBI 2019), IEEE, 2019, pp. 1207–1211.

[10] A.-A.-Z. Imran, A. Hatamizadeh, S.P. Ananth, X. Ding, D. Terzopoulos, N. Tajbakhsh, Automatic Segmentation of Pulmonary Lobes Using a Progressive Dense V-Network, in: D. Stoyanov, et al. (Eds.), Deep Learning in Medical Image Analysis and Multimodal Learning for Clinical Decision Support. DLMIA 2018, ML-CDS 2018. Lecture Notes in Computer Science, vol. 11045, Springer, Cham, 2018, doi:10.1007/978-3-030-00889-5_32.
[11] H. Tang, C. Zhang, X. Xie, Automatic pulmonary lobe segmentation using deep learning, in: 2019 IEEE 16th International Symposium on Biomedical Imaging (ISBI 2019), IEEE, 2019, pp. 1225–1228.
[12] S. Saita, M. Kubo, Y. Kawata, N. Niki, H. Ohmatsu, N. Moriyama, An algorithm for the extraction of pulmonary fissures from low-dose multislice CT image, Systems and Computers in Japan 37 (9) (2006) 63–76.
[13] J.-M. Kuhnigk, H. Hahn, M. Hindennach, V. Dicken, S. Krass, H.-O. Peitgen, Lung lobe segmentation by anatomy-guided 3D watershed transform, in: Medical Imaging 2003: Image Processing, 5032, International Society for Optics and Photonics, 2003, pp. 1482–1491.
[14] S. Ukil, J.M. Reinhardt, Anatomy-guided lung lobe segmentation in X-ray CT images, IEEE transactions on medical imaging 28 (2) (2009) 202–214.
[15] B. Lassen, E.M. van Rikxoort, M. Schmidt, S. Kerkstra, B. van Ginneken, J.-M. Kuhnigk, Automatic segmentation of the pulmonary lobes from chest CT scans based on fissures, vessels, and bronchi, IEEE transactions on medical imaging 32 (2) (2013) 210–222.
[16] X. Zhou, T. Hayashi, T. Hara, H. Fujita, R. Yokoyama, T. Kiryu, H. Hoshi, Automatic segmentation and recognition of anatomical lung structures from high-resolution chest CT images, Computerized Medical Imaging and Graphics 30 (5) (2006) 299–313.
[17] V. Appia, U. Patil, B. Das, Lung fissure detection in CT images using global minimal paths, in: Medical Imaging 2010: Image Processing, 7623, International Society for Optics and Photonics, 2010, p. 76231P.
[18] S. Qi, H.J. van Triest, Y. Yue, M. Xu, Y. Kang, Automatic pulmonary fissure detection and lobe segmentation in CT chest images, Biomedical engineering online 13 (1) (2014) 59.
[19] Q. Wei, Y. Hu, G. Gelfand, J.H. Macgregor, Segmentation of lung lobes in high-resolution isotropic CT images, IEEE Transactions on biomedical engineering 56 (5) (2009) 1383–1393.
[20] L. Zhang, E.A. Hoffman, J.M. Reinhardt, Atlas-driven lung lobe segmentation in volumetric x-ray CT images, IEEE transactions on medical imaging 25 (1) (2006) 1–16.
[21] E.M. Van Rikxoort, M. Prokop, B. de Hoop, M.A. Viergever, J.P. Pluim, B. van Ginneken, Automatic segmentation of pulmonary lobes robust against incomplete fissures, IEEE transactions on medical imaging 29 (6) (2010) 1286–1296.
[22] F.J. Bragman, J.R. McClelland, J. Jacob, J.R. Hurst, D.J. Hawkes, Pulmonary lobe segmentation with probabilistic segmentation of the fissures and a groupwise fissure prior, IEEE transactions on medical imaging 36 (8) (2017) 1650–1663.
[23] M. Kubo, N. Niki, K. Eguchi, M. Kaneko, N. Kusumoto, N. Moriyama, H. Omatsu, R. Kakinuma, H. Nishiyama, K. Mori, et al., Extraction of pulmonary fissures from thin-section CT images using calculation of surface-curvatures and morphology filters, in: Image Processing, 2000. Proceedings. 2000 International Conference on, 2, IEEE, 2000, pp. 637–640.
[24] J. Wang, M. Betke, J.P. Ko, Pulmonary fissure segmentation on CT, Medical Image Analysis 10 (4) (2006) 530–547.
[25] T. Klinder, H. Wendland, R. Wiemker, Lobar fissure detection using line enhancing filters, in: Medical Imaging 2013: Image Processing, 8669, International Society for Optics and Photonics, 2013, p. 86693C.
[26] J. Pu, J.K. Leader, B. Zheng, F. Knollmann, C. Fuhrman, F.C. Sciurba, D. Gur, A computational geometry approach to automated pulmonary fissure segmentation in CT examinations, IEEE Transactions on Medical Imaging 28 (5) (2009) 710.
[27] J. Pu, C. Fuhrman, J. Durick, J.K. Leader, A. Klym, F.C. Sciurba, D. Gur, Computerized assessment of pulmonary fissure integrity using high resolution CT, Medical physics 37 (9) (2010) 4661–4672.
[28] S. Gu, D. Wilson, Z. Wang, W.L. Bigbee, J. Siegfried, D. Gur, J. Pu, Identification of pulmonary fissures using a piecewise plane fitting algorithm, Computerized Medical Imaging and Graphics 36 (7) (2012) 560–571.
[29] A.F. Frangi, W.J. Niessen, K.L. Vincken, M.A. Viergever, Multiscale vessel enhancement filtering, in: International Conference on Medical Image Computing and Computer-Assisted Intervention, Springer, 1998, pp. 130–137.
[30] J.C. Ross, R.S.J. Estépar, G. Kindlmann, A. Díaz, C.-F. Westin, E.K. Silverman, G.R. Washko, Automatic lung lobe segmentation using particles, thin plate splines, and maximum a posteriori estimation, in: International Conference on Medical Image Computing and Computer-Assisted Intervention, Springer, 2010, pp. 163–171.
[31] R. Wiemker, T. Bülow, T. Blaffert, Unsupervised extraction of the pulmonary interlobar fissures from high resolution thoracic CT data, in: International Congress Series, 1281, Elsevier, 2005, pp. 1121–1126.
[32] B. Lassen, J.-M. Kuhnigk, O. Friman, S. Krass, H.-O. Peitgen, Automatic segmentation of lung lobes in CT images based on fissures, vessels, and bronchi, in: Biomedical Imaging: From Nano to Macro, 2010 IEEE International Symposium on, IEEE, 2010, pp. 560–563.
[33] D.P. Shamonin, M. Staring, M.E. Bakker, C. Xiao, J. Stolk, J.H. Reiber, B.C. Stoel, Automatic lung lobe segmentation of COPD patients using iterative B-spline fitting, in: Medical Imaging 2012: Image Processing, 8314, International Society for Optics and Photonics, 2012, p. 83140W.

[34] Q. Li, S. Sone, et al., Selective enhancement filters for nodules, vessels, and airway walls in two-and three-dimensional CT scans, Medical physics 30 (8) (2003) 2040–2051.

[35] G. Papari, N. Petkov, Edge and line oriented contour detection: State of the art, Image and Vision Computing 29 (2-3) (2011) 79–103.

[36] C. Xiao, B.C. Stoel, M.E. Bakker, Y. Peng, J. Stolk, M. Staring, Pulmonary fissure detection in CT images using a derivative of stick filter, IEEE transactions on medical imaging 35 (6) (2016) 1488–1500.

[37] Y. Peng, C. Xiao, An oriented derivative of stick filter and post-processing segmentation algorithms for pulmonary fissure detection in CT images, Biomedical Signal Processing and Control 43 (2018) 278–288.

[38] C. Lopez-Molina, G.V.-D. De Ulzurrun, J.M. Baetens, J. Van den Bulcke, B. De Baets, Unsupervised ridge detection using second order anisotropic gaussian kernels, Signal Processing 116 (2015) 55–67.

[39] P.-L. Shui, W.-C. Zhang, Noise-robust edge detector combining isotropic and anisotropic gaussian kernels, Pattern Recognition 45 (2) (2012) 806–820.

[40] J.-M. Geusebroek, A.W. Smeulders, J. Van De Weijer, Fast anisotropic gauss filtering, IEEE Transactions on Image Processing 12 (8) (2003) 938–943.

[41] R.H. Hardin, N.J.A. Sloane, W.D. Smith, Tables of spherical codes with icosahedral symmetry, published electronically at http://NeilSloane.com/icosahedral.codes/.

[42] M. Reisert, Spherical derivatives for steerable filtering in 3D, IIFLMB, Computer Science Department, University of Freiburg, Tech. Rep. Internal Report 3 (07) (2007).

[43] R. Courant, D. Hilbert, Methods of mathematical physics, New York: Wiley Interscience 1 (1953).

[44] L. Vincent, Morphological area openings and closings for grey-scale images, in: Shape in Picture, Springer, 1994, pp. 197–208.

[45] L. Vincent, Morphological grayscale reconstruction in image analysis: applications and efficient algorithms, IEEE transactions on image processing 2 (2) (1993) 176–201.

[46] H. Skibbe, M. Reisert, Spherical tensor algebra: a toolkit for 3D image processing, Journal of Mathematical Imaging and Vision 58 (3) (2017) 349–381.

[47] Mevislab online available, http://www.mevislab.de/.

[48] Elcap public lung image database, http://www.via.cornell.edu/databases/lungdb.html.

[49] A.P. Reeves, Y. Xie, S. Liu, Large-scale image region documentation for fully automated image biomarker algorithm development and evaluation, Journal of Medical Imaging 4 (2) (2017) 024505.

[50] E. Van Rikxoort, B. Van Ginneken, Automatic segmentation of the lungs and lobes from thoracic CT scans, in: Proc. 4th Int. Workshop Pulmonary Image Anal, 2011, pp. 261–268.

[51] R. San Jose Estepar, J.C. Ross, R. Harmouche, J. Onieva, A.A. Diaz, G.R. Washko, Chest imaging platform: an open-source library and workstation for quantitative chest imaging, in: C66. LUNG IMAGING II: NEW PROBES AND EMERGING TECHNOLOGIES, American Thoracic Society, 2015, p. A4975.